Estimating the refractivity bias of Formosat-7/COSMIC-II GNSS Radio Occultation in the deep troposphere

Gia Huan Pham[1], Shu-Chih Yang[1,2], Chih-Chien Chang[1], Shu-Ya Chen[2], and Chung-Yung Huang[3]

[1]Department of Atmospheric Sciences, National Central University, Taoyuan, Taiwan
[2]GPS Research and Application Center, National Central University, Taoyuan, Taiwan
[3]Taiwan Space Agency, Hsinchu, Taiwan

Correspondence to: Shu-Chih Yang (shuchih.yang@atm.ncu.edu.tw)

Abstract

FORMOSAT-7/COSMIC-2 radio occultation (RO) measurements show promise for observing the deep troposphere and providing critical information on the Earth's planetary boundary layer (PBL). However, refractivity retrieved in the low troposphere can have severe biases under certain thermodynamic conditions. This research examines the characteristics of the deep tropospheric biases and presents methods for estimating the region-dependent refractivity bias using statistical regression models. The results show that the biases have characteristics that vary with land and oceans. With substantial correlation between local spectral width (LSW) and bias, the LSW-based bias estimation model can explain the general pattern of the refractivity bias, but with deficiencies in measuring the bias in the ducting regions and certain areas over land. The estimation model involving the relationship with temperature and specific humidity can capture the large biases associated with ducting. Finally, a minimum variance estimation that combines the LSW and temperature/water vapor models provides the most accurate estimation of the refractivity bias.

1 Introduction

Global Navigation Satellite System (GNSS) radio occultation (RO) observations have become a critical data source in atmospheric applications, particularly numerical weather prediction (NWP) (e.g., Healy, 2008; Rennie, 2010; Cucurull et al., 2007, 2017; Lien et al., 2021). Low-Earth-orbiting (LEO) satellites receive radio signals from GNSS transmitters, which bend due to atmospheric density changes. Information on the bending angle can be obtained with the GNSS RO technique, and then the atmospheric refractivity is further derived by Abel inversion. Since the RO technique measures the signal phase delay, it is not affected by clouds and rainfall. The RO profile is an all-weather observation with a high vertical resolution.

The RO observations, bending angle and refractivity, measure vertical gradients in atmospheric density, a function of temperature, moisture and pressure (Kuo et al., 2004). RO observations provide information on temperature (stratosphere and upper troposphere) and moisture (lower troposphere) with low noise and low systematic errors (biases), which makes them useful in atmospheric research (Eyre, 2008). Several GNSS RO missions, e.g., the FORMOSAT-3/Constellation Observing System for Meteorology, Ionosphere, and Climate (FS3/C), FORMOSAT-7/COSMIC-2 (FS7/C2), Meteorological Operational satellite (MetOp), Gravity Recovery And Climate Experiment (GRACE), Satellite de Aplicaciones Cientifico-C (SAC-C), X-band TerraSAR satellite (TerraSAR-X), Korea Multi-Purpose Satellite-5 (KOMPSAT-5), etc., have provided much RO data for NWP.

Many studies have illustrated the positive impact of assimilating RO observations, such as the operational forecast systems at the European Centre for Medium-Range Weather Forecasts (ECMWF) (Healy, 2014), the NCEP/Environmental Modeling Center (EMC) (Cucurull, 2007) and the Taiwan Central Weather Administration (CWA) (Lien et al., 2021). Moreover, studies have been initiated recently to investigate the potential of assimilating the large volume of commercial RO data from Spire, and the benefits can be identified in weather forecasting (Bowler, 2020a). In addition to improving global NWP, studies have also confirmed that assimilating RO observations improves severe weather prediction, particularly for tropical cyclones and heavy rainfall (e.g., Chen et al. 2020; 2021a,b, 2022; Chang and Yang, 2022; Yang et al., 2014).

As the successor of FS3/C, the FS7/C2 mission was launched in 2019 with support from the Taiwan National Space Agency (TASA) and the United States National Oceanic and Atmospheric Administration (NOAA) and National Science Foundation. The number of profiles obtained by FS7/C2 is approximately three times greater than that of FS3/C since FS7/C has dense coverage over the tropics and subtropics (Chen et al., 2021c). Compared with FS3/C, FS7/C2 has a higher signal-to-noise ratio (SNR), wider bandwidth, and a better open-loop (OL) tracking model. These advantages enable the retrieval of more data from RO signals penetrating the moist troposphere and having the ability to detect the planetary boundary layer (PBL) and superrefraction (SR) over the top of the PBL (Schreiner et al., 2020; Sokolovskiy et al., 2024). Chen et al. (2021c) showed that the data availability of the FS7/C2 RO profiles under 1km is five times greater than that of the FS3/C profiles over a six-month range. Anthes et al. (2022) noted that the penetration rate of RO profiles is high even under extremely moist conditions and near tropical cyclones. The ability to penetrate deep into the atmosphere makes RO measurements ideal for studying the PBL. The PBL is directly influenced by any exchange of energy, momentum and mass between Earth's surface and the atmosphere, and thus its characteristics are crucial for weather and climate variabilities.

However, the use of GNSS RO in the lower atmosphere still has errors when radio rays pass through areas with strong vertical or horizontal refractivity gradients. It is known since 1997 that negative biases in refractivity exist in the lower troposphere, especially in the tropics (Rocken et al. 1997). The implementation of open-loop tracking (Sokolovskiy, 2001) and the use of the holographic retrieval method largely reduce the negative refractivity bias (REFB) in lower troposphere in earlier generation RO missions. The "radioholographic" methods such as the canonical transform (CT) method (Gorbunov, 2001, 2002), Full Spectrum Inversion (FSI) (Jensen et al, 2002) and Phase matching (PM) (Jensen et al, 2004) largely solve the multipath issue resulting from the "strong" refractivity gradient. Still, negative REFB can arise in deep troposphere from multiple causes, as summarized by Feng et al. (2020) and Wang (2020). A common cause (but not the only one) of negative biases in the lower troposphere is ducting (Sokolovskiy 2003; Ao et al. 2003; Xie et al. 2010). When the vertical gradient of refractivity $\partial N/\partial z$ exceeds a critical value of -157 N units per km (Lopez 2009), ducting occurs and rays are trapped inside the ducting layer. In the presence of ducting, the singularity problem in the Abel transforms leads to a non-unique inversion problem. Thus, the Abel inversion results in a negatively bias refractivity below the ducting layers (Sokolovskiy, 2003). Feng et al. (2020) reported that climatological locations agree well with the areas of high ducting frequency, mainly over the subtropical eastern oceans. Furthermore, there are non-ducting related biases exist in the RO data. Error associated with low SNR in the complex moist lower troposphere may cause negative biases in bending angles and refractivity. Another potential source is the propagation of radio waves in a medium with random refractivity irregularities can also cause biases (Gorbunov et al. 2015). In regard to the assimilation of RO data, quality control (QC) is applied to reject the RO data if the observation or the corresponding backgrounds are suspected to be affected by superrefraction. The rejection rate is high below 2 km due to the negative bias, which could also discard valuable information for data assimilation. To increase the value of RO data in the lower atmosphere, this study aims to examine the characteristics of the REFBs with the FS7/C2 RO data in more detail and proposes methodologies to estimate them.

Previous research has demonstrated that the negative REFB in the ABL can be recognized and estimated using canonical transform approximations (Sokolovskiy, 2003) and can be reconstructed in the presence of ducting conditions (Xie et al., 2006). Based on Xie et al. (2006), Wang et al. (2017) developed an optimal estimation of negative bias using precipitable water (PW) observations from Advanced Microwave Scanning Radiometer from the EOS (AMSR-E) microwave radiometer satellite data. Wang et al. (2020) further proposed a bias estimation algorithm by generating a candidate set of modeled ducting profiles. The one with the vertical gradient of the reflected bending angle closest to the observed profile is taken as the bias-corrected profile. However, there are some limitations with these methods, such that they only correct for ducting-related bias and the grazing signal of the bending measurement is needed. For the RO observation error, the local spectral width (LSW), which measures the uncertainty of the RO bending angle, has been used to indicate the quality of the individual RO profiles. The LSW represents the errors caused by the nonspherical symmetry of refractivity in the moist troposphere (Gorbunov, 2006; Sokolovskiy 2010). The LSW parameter has improved the use of RO observations in data assimilation, including in the QC procedure (Liu et al., 2018) and dynamic estimation of RO error in the lower troposphere (Zhang et al. 2023). Liu et al. (2018) showed that both uncertainties and biases were related to LSW. Sjoberg et al. (2023) recently showed a strong statistical correlation between lower tropospheric uncertainties and LSW. They also mentioned that they found a correlation between biases and LSW as well, but did not provide details. Furthermore, Bowler (2020b) proposed estimating RO errors with information on mean temperatures below 20 km. These results suggest that variations in LSW, temperature and humidity are related to the bias. Thus, we developed statistical models that adaptively consider the biases associated within each RO profile using LSW and temperature and water vapor.

We first investigate the characteristics of the FS7/C2 RO REFB and establish regression-based bias estimation algorithms. Two types of algorithms are examined. One is based on the physical LSW parameter, and the other is related to thermodynamic variables (temperature and water vapor). By comparing the results of the estimated bias, we can identify how they link to the characteristics of each participating variable. Finally, a bias correction method for the RO profile in the lower troposphere is proposed by combining the two error estimation algorithms. We expect that this new algorithm can be used in different aspects such as improving the products of temperature and moisture profiles retrieved from the refractivity in the moist lower troposphere (Chen et al. 2020), definition of the PBL height (Xie, 2014), and the estimation of precipitable water vapor (Yeh et al. 2024). Furthermore, for the DA systems that assimilate the RO refractivity, it is expected that the RO data in the deep troposphere can be better exploited by using the bias estimation as a QC flag or assimilating the calibrated refractivity profiles.

The remaining portions of this paper are organized as follows. Section 2 provides the data information and methods for estimating the refractivity bias. Section 3 discusses the general characteristics of bias and its sensitivities with respect to different variables and land/sea conditions. Section 4 presents the results of bias estimation algorithms. Finally, the summary and conclusion are provided in Section 5.

2. Data and methodology

2.1 GNSS RO FS7/C2 and ECMWF data

This study uses the FS7/C2 RO atmospheric profiles (atmPrf) and wet products (wetPf2) processed by the Taiwan Data Processing Center (TDPC). The study period is from 1st December 2019 to 29th February 2020, before the FS7/C2 data were assimilated in the ECMWF analysis. All RO profiles are distributed between 45°S and 45°N due to the low inclination orbits of the FS7/C2 satellites. A total of 244,853 profiles are selected with the flag of "good data" during the periods, and only data below the height of 25 km are used to focus on the bias characteristics in the troposphere. The data quality of the FS7/C2 constellation is improved compared to FS3/COSMIC (FS3/C) due to the use of the advanced RO receiver and postprocessing with open-loop tracking. Most of the profiles show a deeper penetration with depths below 1 km, and the penetration rate is 40% higher than those of FS3/C (Chen et al., 2021c). Figure 1 shows the number of profiles that penetrate below 1.5 km above the mean sea level (MSL) during the selected periods. The FS7/C2 data are mostly in tropical areas and have more profiles penetrating below 1.5 km over oceans than over land.

The ECMWF atmospheric reanalysis (ERA5, https://www.ecmwf.int/en/forecasts/access-forecasts/access-archive-datasets) is used as the reference RO profiles. The hourly ERA5 reanalysis in the study period has a horizontal resolution of 0.25 x 0.25 deg with 37 pressure levels, ranging from 1000 to 1hPa. The variable geopotential, temperature and specific humidity are selected. Since the time of the RO data is precise in minutes, we rounded the time of the RO profiles to the nearest hour. The ERA5 profiles are derived by interpolating the reanalysis horizontally and vertically to the location and vertical levels of the RO atmPrf. The RO REFB is defined as the difference between the FS7/C2 and the ERA5 RO observations at each level. This assumes that the ERA5 refractivities are close to truth. These biases are referred to as the real biases in this paper. Nevertheless, it is possible that ERA5 may carry its own biases, which will not be discussed in this study.

For constructing the statistical models, the predictors are LSW, temperature (*T*), and specific humidity (*Q*). The LSW, available in the atmPrf data, are calculated from the width of the spectrum during the RO processing (Liu et al. 2018). The *T* and *Q*, available in the wetPf2 data, are computed from a one-dimensional variational (1D-Var) retrieval algorithm using ECMWF 12-h forecast as the a priori (Wee at al. 2022).

2.2 Statistical models for bias estimation

Two polynomial regression models are developed to estimate the REFB using predictors associated with different attributions of the observational error in GNSS RO data. The first model uses LSW/2 as the predictor, and the other uses temperature (*T*) and specific humidity (*Q*) as the predictors. Liu et al. (2018) used a linear function of LSW/2 to illustrate the FS3/C dynamic error variance in the bending angle and refractivity, and the scaling factor 1/2 for LSW approximates the root mean square of random error of the bending angle (Liu et al. (2018), assuming a Gaussian spectrum (Sirmans and Bumgarner 1975). Following Liu et al. (2018), we use the variable LSW/2 and modify this relationship to a polynomial regression. The other bias estimation model is established using the thermodynamic variables to emphasize the impact of the thermodynamic structure on REFB in deep troposphere. The two polynomial regression models are referred to as the LSW and *TQ* estimators, respectively. The LSW represents the RO inversion uncertainty, and *T* and *Q* represent the impact of the thermodynamic structure on REFB within the ABL. Each of these variables is expected to partly explain the characteristics of the bias.

In each estimator, the order of the polynomial is optimized by using the metrics of R-squared and mean square error to assess the goodness of the fitting performance. The polynomial regression is performed with the training data, which is 80% of the total data, and the rest (20%) of the data is used for evaluating the regression performance. To derive a robust regression model, independent regression fitting is repeated five times by replacing the training/testing data with a different 80%/20% subsets of the data so that the testing data from five experiments eventually covers the whole data set. The regression model with the best fitting performance for both training and testing data is chosen as the optimal one. Given that our goal is to construct regional-dependent estimators to consider the spatial variation in the REFB, we group the RO refractivity profiles from 45°S to 45°N into 5°longitude x 3° latitude boxes (Figure 1), and the regression-based REFB estimators are built in each box. In total, there are 72 x 30 boxes. The boxes are defined by considering the number of available RO profiles below 1.5km should be at least 10 profiles in each box for conducting the regression training and testing. With the 3 months of data used in our study, choosing testing data lower than 20% of the total data results in a very coarse resolution of the boxes. On the other hand, choosing any number larger than 20% would sacrifice the amount of data that can train a reliable regression model. We note that all profile data below 1.5 km are used first (80% for training and 20% for testing) to determine the order of the LSW-based regression model and the optimal combination of the multi-variable (*T* and *Q*) regression model.

For the LSW estimator, a second-order polynomial is chosen based on the R-squared metric. Afterwards, a second-order polynomial regression is constructed for an individual box. Eq. (5) shows the formula of the LSW estimator in the i_{th} box

$$u_i = \alpha_{i,1}x_i^2 + \alpha_{i,2}x_i + \alpha_{i,3} \tag{1}$$

where u_i, the predictand, is the REFB, x_i is the LSW/2, and $\alpha_{i,*}$ are the regression coefficients. Although the biases related to the signal tracking or multipath is much reduced after with the implementation of open-loop tracking and radio-holographic retrieval method, we expect that LSW can partially capture the biases inherited from bending angle.

A similar procedure is applied to derive a multivariable polynomial regression model with *T* and *Q* obtained from the 1D-Var analysis of the RO wet products (Wee et al. 2022) as the predictors. For consistency, the real REFB originally defined with the atmPrf, will be interpolated to the same levels of the wetPf2. No REFB, *T* and *Q* are collected if the *T*, *Q* profiles terminate above 1.5 km MSL. Before fitting, *T* and *Q* are standardized as

$$\chi = \frac{x_i - \min(x_i)}{\max(x_i) - \min(x_i)} \tag{2}$$

where χ represents a normalized quantity ranging between 0 and 1 and x_i is the original value of Q or T in the i^{th} box. Given two variables, there are different combinations of order and interaction terms (multivariable polynomial function has the form of $\sum_{m=0}^{m=M}\sum_{l=0}^{l=L} b_{m,l}y^m z^l$, where *m* and *l* are the order of variable *y* and *z*, respectively, and $b_{m,l}$ is the regression coefficient). For this application, the mean squared error is used to determine the optimal fitting formula given that R-squared are comparable when higher order terms are included. The optimal multivariable polynomial regression model has the form:

$$u_i = \beta_{i,1} y_i^2 + \beta_{i,2} y_i + \beta_{i,3} y_i z_i \tag{3}$$

where u_i is REFB, y_i is the normalized Q, z_i is the normalized T and $\beta_{i,*}$ are the regression coefficients. Considering the quadratic term of moisture is essential. The R-squared (MSE) value increases (decreases) from 0.535 (37.044) with the y_i and $y_i z_i$ terms to 0.732 (26.610) with the y_i^2 term.

We further apply the minimum variance estimation (MVE, Clarizia et al., 2014) to combine the results from the LSW and TQ estimators. This approach has the advantage of having a smaller RMS error than either the LSW or TQ estimation. The MVE is built to linearly combine the estimations so that the new estimation has the minimum error variance:

$$u_{i,MVE} = \mathbf{m} \cdot \mathbf{u} \tag{4}$$

where **u** is the vector of individual estimated refractivity bias and **m** is the vector of combination coefficients. One of the advantages of this combination is that **m** is derived considering the error covariance matrix of individual bias estimators.

$$\boldsymbol{m} = \left(\sum_{i=1}^{K} \sum_{j=1}^{K} c_{i,j}^{-1}\right)^{-1} \mathbf{C}^{-1} \mathbf{1} \tag{5}$$

where $\mathbf{1}$ is a vector with all elements equal to one, K is the dimension of $\boldsymbol{m}$ ($K = 2$ in our application), $\mathbf{C}^{-1}$ is the inverse of the covariance matrix between the individual estimation errors and $c_{i,j}^{-1}$ are the elements of $\mathbf{C}^{-1}$.

The element of the error covariance matrix **C** is expressed as $\boldsymbol{c_{i,j}} = \langle (\boldsymbol{u_i} - \boldsymbol{u_t})(\boldsymbol{u_j} - \boldsymbol{u_t}) \rangle$, where u_i and u_j is the i^{th} and j^{th} bias estimation, respectively, and u_t is the real bias.

3 Characteristics of the refractivity bias

3.1 General characteristics of REFB

Figure 2a shows the profile of the averaged REFB and its standard deviation from 0-25 km. RO data have significant biases in comparison to the ERA5 reference, especially in the low troposphere. The bias is evident below 5 km and is largest at the surface with an amplitude of approximately -11 *N*-units. Given the large variations in moisture and temperature in the low troposphere, the standard deviation below the 2 km height increases as the height decreases. Notably, although the total number of profiles quickly decreases below 5 km (Fig. 2b), there remain enough data for near-surface statistical evaluation, with about a 40% penetration rate at 0.5 km in reference to the total number of profiles at 10 km (Fig. 2c). The mean LSW (red line in Fig. 2a) also increases sharply as the height decreases, with two peaks, at the surface and near 2 km.

Figure 3a shows the latitudinal cross-section of the REFB. The largest values of REFB are below 5 km in the subtropics and tropics and slightly shifted to the Southern Hemisphere due to the austral summer. The opposite pattern, which has a high bias shifted to the Northern Hemisphere, is also seen with the data from June to August 2020 (not shown). This result indicates the general dependence of the distribution of REFB on the seasonal temperature and water vapor structure. Similar to the REFB pattern, large LSW occurs mainly in the tropics, tilting toward the Southern Hemisphere with the maximum near the surface (Fig. 3b). This finding illustrates that LSW variation can be related to the REFB to some extent. Moreover, other high LSW values are located a few kilometers above the surface of the Southern Hemisphere. The increased LSW above 2 km could be caused by common inversion layers in the troposphere of some oceans (Sokolovskiy et al. 2014). Another effect that could be considered is the influence of convective clouds just above moist oceans (Yang et al., 2016). The large LSW near the surface in Fig. 3b reflects the ability of FS7/C2 to penetrate deep into the moist troposphere of the tropics. However, this surface maximum was not seen in the study of Zhang et al. (2023) using FS3/C data in August 2008.

3.2 Dependence on geography and thermodynamic conditions

We further examine the dependence of the REFB on land and oceanic thermodynamic conditions. Figure 4 compares REFB between land and ocean, together with its standard deviation (stdv) and LSW. Both REFB and LSW below 4 km are somewhat larger over oceans, and the REFB extends to higher altitudes (Fig. 4c vs. 4d) with a greater vertical gradient of REFB below 2 km. The magnitudes of mean REFB and stdv above 2 km are comparable over land and ocean. The shape of the LSW profiles is different over oceans and land, with the second peak value at 2 km more pronounced over oceans. Below 1.5 km, the shape of the REFB profile exhibits characteristics as the LSW profiles, suggesting the potential of LSW as a predictor for estimating REFB.

Given the large REFB in deep troposphere, we focus on the regional variations in REFB averaged below 1.5 km. Figure 5a shows that the averaged value of negative REFB below 1.5 km is largest over the oceanic regions near the western coasts of the South American and African continents. Small negative REFBs appear over the tropical Pacific and land. There are small positive REFBs over the high mountain regions. The different behavior of the REFB over ocean and land implies the impact of regional variability and the associated thermodynamic structure in the lower troposphere. As shown in Fig. 5b-5d, high LSW occurrence is mainly located over the warm equatorial regions of the Pacific, Atlantic and Indian Oceans. However, not all of the regions with high temperature and moisture coexist with the regions with high LSW. Some exceptional regions can be seen, such as offshore to the coast of Southwest Australia and offshore of Southwest Africa near the international data line. Fig. 5 suggests that although LSW, temperature and specific humidity have certain cross-relationships, the characteristics of thermodynamic conditions cannot fully explain the distribution of LSW. Therefore, an REFB estimation model, which is based on only one variable, is not enough to explain REFB.

To further highlight the characteristics of REFB under different conditions, the REFB profiles are grouped according to each profile's LSW, temperature and specific humidity averaged below 1.5 km for land and ocean (Figure 6). As Xie (2014) reported, the 1.5 km MSL is the global mean PBL height calculated from the FS3/C refractivity data. In general, it is evident that the negative REFB increases with increasing LSW below 4 km, as shown in Fig. 3; however, the characteristics are different for land and ocean. Over land, the very high LSW does not guarantee the occurrence of a large REFB in lower troposphere. Moisture and temperature likewise exhibit the same linear relationship with negative REFB in the lower troposphere. However, negative REFBs also tend to occur under conditions of low moisture over the ocean. Figure 6 reveals that the relationship between REFB and LSW, T and Q under 1.5 km is dominantly linear; however, the REFB variations can be further explained by a quadratic relationship with Q. It is noted that REFB at about 10 km increase with increasing LSW, T and Q over both land and oceans, and even become weakly positive at high values of LSW, T and Q averaged below 1.5km. In particular, RO profiles over land with large LSW below 1.5km has the largest positive REFB, nearly 8 N-unit, aloft. Taking only the RO profiles penetrating 0.5 km will modify the characteristics of Figure 6 in two aspects. First, the REFB below 10 km becomes positive for LSW/2 larger than 28%. Second, the REFB for cold temperature shows negative at 15 km. The former feature is related to the early cutoff height in the tropical occultation over central Africa (Sokolovskiy, 2010). The latter feature is attributed to the inversion associated with the large-scale subsidence near the tropopause near mid-latitude. Sensitivity tests to address sampling issues will be discussed in subsection 4.2.

4 Results of bias estimation

4.1 General performance

In this section, we present the estimation for REFB using the methods introduced in Section 2. As mentioned, LSW/2, which represents the retrieval uncertainties of the bending angle and, hence, refractivity uncertainties, is the predictor for the first bias estimation model. The T and Q retrieved from FS7/C2 RO data are the predictors for the second estimator. Although the T and Q products retrieved from RO profiles using 1D-Var retrievals may have errors, they still provide valuable information for REFB estimation through the training process, as described in Section 2.

Figure 7 shows the relationship between the REFB and LSW/2 averaged below 1.5 km for the Southern Hemisphere (SH) and Northern Hemisphere (NH). REFB is grouped every 2% of LSW/2, from 0 to 36%. The solid and dashed lines show the LSW-based REFB estimates for ocean and land, respectively. Under 1.5 km, the magnitude of the negative REFB as a function of LSW is larger over oceans than for land. Generally, as LSW/2 increases, the REFB becomes more negative below 1.5 km for both land and ocean. Although the relationship is dominated by a linear trend, the quadratic term further improves the regression fitting. As shown in Table 1, the correlations over ocean and land are robust (larger or close to 0.9) and similar with the training and testing data in SH and NH. Compared to the REFB under the warm and moist condition of the austral summer in SH, the REFB over NH is weaker but the relationship between LSW/2 and REFB is still strong over ocean and land, except that the one over land has a somewhat stronger quadratic feature. Given this strong relationship, we expect that the relationship during the boral summer season will hold as well. However, the relationship between REFB and LSW/2 is not present above 1.5 km, and there is little difference in REFB between land and ocean.

Figure 8 shows the result of the second bias estimator, which relates the REFB with normalized Q (y) and product of normalized T and Q (yz) under 1.5 km. The TQ estimation over ocean and land captures the feature where the REFB becomes more negative under moist conditions. Similar to the LSW estimator, the TQ estimator shows a stronger dependence over the ocean. The multivariable regression has correlation coefficients equal to 0.79 and 0.72 for ocean and land in SH, respectively, and 0.75 and 0.69 in NH. In general, the REFB shows a robust bi-linear relationship with y and yz, and the quadratic term (y^2) provides further adjustment. With a fixed specific humidity, lower temperature results in larger negative REFB. In Fig. 8a, this result reflects the condition over the cool SST (Fig. 5a and 5d), west of the coast of South America and South Africa. The relationship becomes more linear in NH (Fig. 8a vs. 8c), i.e. less dependence to the quadratic term of specific humidity. For dryer conditions, the *TQ* estimator tends to give neutral to positive REFB, especially over land (Fig. 8b and 8d) where more data are in the dry condition and part of them are over the mid-latitude continent (Fig. 5c). Given a fixed *TQ* value (*yz*=0.5) in Fig. 8, Figure 9 shows the strong relationship between REFB and *Q*. Large negative REFB corresponds to moist condition, but the negative amplitude is larger over the SH ocean with larger variation. The relationship is more quadratic over ocean than over land and is most linear over the NH land. In Figure 8, a slightly positive REFB is estimated for very cold and dry condition over ocean. In Feng et al. (2020), positive REFB is identified in Bering Ocean at high latitude. While Fig. 8 qualitatively suggests the potential to capture such positive REFB over high-latitude, whether the regional-dependent *TQ* estimator can be adequately applied to estimate REFB in the polar or high-latitude regions is still an open question since the FS7/C2 data RO data used in this study mostly distributed in the tropic to subtropic regions.

Figures 7 and 8 confirm that models with LSW/2 or *TQ* as predictors can estimate the REFB under 1.5 km, but there are different sensitivities for ocean and land. In the next step, we further apply these regression methods using the data in 5°longitude × 3°latitude boxes within 45°N to 45°S to construct the region-dependent bias estimation model.

Figure 10 shows the horizontal distribution of the mean real and estimated REFBs with the training and testing data. Notably, there are some differences between the training and testing data (Fig. 10a vs. 10b), such as the large REFB off the western coast of South American and coast of Australia. In comparison to the real REFB distribution (Fig. 10a), the LSW-based REFB (Fig. 10c) captures the general pattern with larger biases over ocean and lower biases over land in both the training and testing data. However, the LSW-based REFB is less capable of capturing the large bias over the subtropical oceans off the west coast of South America and South Africa and Australia. Those are expected to be the oceans that have a cold SST, where ducting occurs commonly due to the frequent occurrence of inversion layers on top of the cool sea surface. Although the LSW-based REFB can also represent a portion of the negative REFB in these regions in general, it is obvious that the values are underestimated there. The LSW-based estimation exhibits good performance in estimating the negative REFB in the Indian Ocean, where the pattern and magnitude of the estimated REFB are close to those of the real REFB. In contrast to the LSW-based REFB, the *TQ*-based REFB represents the large negative REFB in the high-ducting-occurrence regions well. Although the magnitude of the *N*-REFB offshore the coasts of South America and South Africa is still underestimated, the pattern and amplitude of the negative REFB are much better represented in comparison with the LSW-based estimation.

The *TQ*-based estimation (Fig. 10 e,f) captures the low bias pattern well, such as the tropical western Pacific, western South America and Africa, while the LSW-based estimation overestimates the negative bias. The similar pattern between the real and *TQ*-based estimated REFBs can be explained by the following two reasons. The first reason is the ability to capture SST characteristics. For example, cold SST regions can result in a cool, low moisture near-surface atmosphere (Fig. 5c and 5d) and impact the boundary layer. Second, the bias in the RO refractivity profiles will be translated to the 1D-Var *T* and *Q* retrievals.

The final method, the MVE, combines the LSW and *TQ* estimations. As described in Section 2, the MVE derives the optimal combination by considering the error correlation between the individual estimations. Notably, the MVE approach requires knowledge of the error covariance matrix between two components (the matrix **C** in Eq. 5). The error correlation of the two REFB estimators is 0.294. A high error correlation indicates a dependency between the two components and thus there is less benefit from using the MVE method. Although LSW is known to have a relationship with temperature and water vapor, our results indicate that the error correlation between two estimates is low enough that it is expected that the MVE can extract useful information from both estimations. Compared to the LSW and *TQ* REFB estimation, the results of the MVE show a pattern closer to the real REFB with both the training and testing data sets.

We next show the root-mean-square error (RMSE) between the real and estimated REFB in each box. Figure 11 shows the contribution of each estimation in estimating bias for land and oceans and reflects the representativeness of the mean REFB shown in Fig. 10. The LSW-based estimation exhibits high RMSE in the cold SST regions and several ocean regions, such as the Southeastern Atlantic, Southeastern and North Western Pacific Oceans, while the *TQ* estimation successfully mitigates this issue. On the other hand, the LSW-based estimation performs better in the tropical Atlantic and Indian Oceans. With training and testing data, the large RMSEs in the LSW or *TQ* estimation over the oceans are largely removed by the MVE method; however slight degradation is observed over the continents of south America and middle Africa. With the testing data (the right column in Fig. 11), the RMSEs are larger in individual estimations, as expected. In general, the MVE method retains its advantage in the optimal estimation over ocean, with an RMSE smaller than that of either estimation. Table 2 shows the global mean RMSE. The *TQ* method has a smaller RMSE compared to the LSW estimation. The MVE method further improves the *TQ* method by 32% and 23.6% with the training and testing data, respectively.

However, we also observed that the *TQ*-based REFB has larger RMSE in the ducting region in southeast Pacific and Atlantic (Fig. 11e vs. Fig. 11f). This is attributed to an overestimated negative REFB (Fig. 10e vs. 10f) by the *TQ* estimator with a much moister near-surface condition in the testing data than those in the training data. The overestimation of the testing data in the ducting regions suggests that more data is required to train the statistical model applicable to a broader range of temperature and moisture requires.

4.2 Sensitivity experiments

This subsection discusses the sensitivity of the REFB estimation to the penetration rate of the RO profiles and investigates the impact of sampling error on constructing the LSW-based and *TQ*-based estimators. Two sets of sensitivities are designed. For the first set of sensitivity, it is required that, in each box, at least 30 RO profiles penetrate a certain level. For the second set of sensitivity, the REFB estimators are obtained for RO data from different levels.

Figure 12 shows the REFB estimation with the testing data using different criteria of the penetration rate. The estimators are obtained when there are at least 30 profiles whose minimum level is smaller than 1.5 or 0.5 km, respectively. The criteria are referred to as CT1 and CT2 in Fig. 12. As the criterion becomes more stringent, more samples in the tropics are rejected and insufficient samples are available in the core of the ducting regions and areas with latitudes higher than 30 degrees. For boxes with sufficient samples with the CT2 criterion, the patterns of REFB, LSW, *T* and *Q* (the right column in Fig. 5) are very similar to the ones with an eased standard criterion, but their amplitudes are generally higher. Nevertheless, the real REFB in Fig. 12a and Fig. 12b is very similar to that in Fig. 10b using an eased criterion on sample number. This similarity is due to fact that the data amount between 0.5 and 1.5 km is much more than that below 0.5km (Fig. 2b). However, the real REFB with CT2 is larger in south Pacific and Atlantic. This reflects that the REFB quicky increases near the surface (Fig. 3a), which can be emphasized after the RO profiles with early termination are removed. The LSW-based REFB with strict criteria also captures the general pattern of real REFB, while the *TQ*-based REFB captures the large negative REFB in the ducting regions well. The REFB estimation using the C2 criterion still show good ability in the regions that the real REFBs are somewhat different between the C2 and standard criteria, such as Central and northwestern Pacific. This good performance is attributed to the fact that the region-dependent regression models can adapt to the changes in the training data in boxes.

Based on the results in Fig. 12, we separate the REFB estimation to different vertical levels, below 0.5 and between 0.5 and 1.5 km (Figure 13). As shown in Fig. 3b, the real REFB below 0.5 km is generally larger than that between 0.5 and 1.5km, except for western Pacific and the ducting regions, west of south America and south Africa. Below 0.5km, the penetration rate declines quickly, reducing the sample size. Nevertheless, it is shown that both REFB estimators perform well in estimating the REFB as well, in particular that the *TQ*-estimator is good at capturing the large REFB. Both estimators can even capture the large negative REFB in central southern Pacific and south India, and the MVE REFB improves the *TQ*-based REFB in central Pacific (150°W to 150°E). However, the *TQ*-estimator provides positive REFB estimation in the cold and dry condition north of Africa, while a weak negative value is exhibited in the real REFB. While the *TQ*-estimator is very sensitive to the amplitude of temperature and moisture, we emphasize that the regression model may not be reliable with a limited sampling size in mid-latitude regions. Results of the REFB estimation between 0.5 and 1.5 km are very similar to Fig. 10. This again confirms that the REFB shown in Fig. 10 is dominated by the data between 0.5 and 1.5 km. Nevertheless, it is important that both REFB estimators can reflect not only the general characteristics and also the differences at different vertical levels.

4.3 Estimating vertical profiles of refractivity bias

This section examines the performance of the REFB estimation methods and whether they can be used for estimating the vertical profiles of REFB. The following three areas (indicated in Fig. 9a) with different REFB characteristics are selected as examples: Area A is in the region of 0° < Lat < 10°N and 55°E < Lon <75°E, Area B is in the region of 20°S < Lat < 30°S and 105°W < Lon < 85°W, and Area C is in the region of 35°S < Lat < 45°S and 120°W < Lon < 135°W. For each area, the estimated REFB at different levels are derived using the estimation methods defined in the previous section. Figure 14a-c shows the mean of the real and estimated REFB profiles in three areas with the testing data. We note that the results of the training and testing data are very similar. In Area A, the mean negative REFB is large at the surface but gradually reverses to a positive bias at 3 to 5 km. In this case, the air below 2 km is very warm and moist over the Indian Ocean (Fig. 14d). The highly humid condition gives a large LSW (Fig. 5b and 5c), and thus, the LSW method can have a good ability to estimate bias in this circumstance, while the *TQ* method overestimates the negative REFB. In contrast, Area B shows different patterns (Fig. 14b): the real negative REFB is even larger (-17 N units) at the surface, and the negative bias at 2 km is still large compared to that in Area A. As shown in Fig. 14d, this characteristic is associated with the inversion layer at 2 km over the cold SST region and large vertical moisture gradient, a typical condition of ducting. While the LSW-based estimation underestimates the negative REFB with the existence of the inversion layers this can be captured by *TQ*-based estimation. Nevertheless, the MVE method is always much closer to the real REFB. In Fig. 14b Area B shows the improvement in the MVE than the *TQ*-based estimation, while large RMSE remained in Area B with the MVE method in Fig. 11f. It should be noted that Fig. 11 is calculated based on the difference the real REFB and estimated REFB of each profile “averaged” below 1.5 km, where Fig. 14 groups the profiles with an interval of 500m. Therefore, the overestimation REFB below 1km with the *TQ*-based estimator is alleviated with the average data used to construct Fig. 11.

For the box located offshore of north America with the mid-latitude cold and dry condition (Fig. 14c), both estimators capture the general pattern of the vertical distribution of REFB but the amplitude below 1 km is smaller than the real REFB. Nevertheless, the *TQ*-based REFB is much better represented compared to one from the LSW estimator. Fig. 14 suggest that both estimators can be applied to estimate the vertical variations of REFB in different regions. However, sample issues may be encountered in mid-latitude regions as discussed in section 4.2.

5. Conclusions

This study investigates the characteristics of refractivity bias (REFB) of FS7/C2 and its sensitivities to RO measurement uncertainty (LSW) and thermodynamic conditions (temperature and moisture). Two bias estimation models are constructed based on polynomial regression with the LSW, and temperature and specific humidity are used as predictors in each estimation. The study period is December 2019-February 2020, with the ERA5 reanalysis data taken as the reference truth.

Similar to previous studies, the low-level FS7/C2 RO refractivity data of during the study period contain significant biases when compared with ERA5. In general, the REFB below 1.5 km is negatively proportional to LSW and exhibits a stronger dependency over ocean than over land. Additionally, REFB in the PBL has a strong dependence on low-level temperature and moisture. While the majority of Pacific and Indian Oceans with warm SSTs have significant negative REFBs, the largest negative REFB regions are near the cold SST regions off the western coasts of South America and South Africa. Small and even positive REFBs are observed over South America and South Africa.

Two REFB estimation models based on the polynomial regression approach are first applied to construct the region-dependent mean REFB below 1.5 km. One estimation model uses a quadratic function of LSW. The other uses the multivariable polynomial regression with temperature and specific humidity (*TQ*) as predictors, and the moisture variable become emphasized after optimization. The estimation models are then applied to 72×30 boxes from 45°S to 45°N. The minimum error variance (MVE) method is used to combine two REFB estimations. The results show that the bias estimation models with either LSW or *TQ* have their own advantages in estimating REFB. The LSW-based model shows the ability to capture the general pattern of the negative REFB but the amplitude is significantly underestimated in the ducting areas. The *TQ*-based model has great performance in representing the pattern and amplitude of REFB, particularly the large negative REFB in the ducting areas and small REFB over most land regions. While the relationship between REFB and LSW below 1.5km is very strong in a global sense, the *TQ*-based REFB shows its advantage in capturing the regional characteristics. The MVE estimation successfully adopts the advantage from either LSW or *TQ* estimation and has the smallest RMSE, particular over ocean.

Results of sensitivity tests show that the estimators at mid-latitude could be affected by the sampling issue since requiring profiles penetrating 0.5 km cannot obtain sufficient samples to construct the regression models. With the 3 months of data, the REFB estimation in tropic to subtropic regions remains similar with the RO profiles penetrating below 1.5 or below 0.5km given that the amount of RO data between 0.5 and 1.5 km dominates. Nevertheless, both the LSW and *TQ* estimation can capture the characteristics of REFB when the RO data are separated to below 0.5 and between 0.5 and 1.5km. Such an ability allows the three REFB estimation models to be applied to reconstruct the REFB vertical profiles for regions with distinct thermodynamic condition in deep troposphere. Both the LSW and *TQ* estimations can well represent the vertical gradient of the mean REFB and the MVE estimation gives an estimated REFB profile closest to the real REFB with the probability distribution similar to the distribution of real REFB.

We should note some of the limitations of these REFB models. The temperature and moisture from the ERA5 reanalysis may have bias. In addition, REFB may have more characteristics regarding smaller scales spatiotemporally. We should also emphasize that the FS7/C2 RO data are mainly located in the tropic to subtropic regions. Therefore, we need more data to justify whether the regression-based bias estimation is applicable in the high-latitude regions. At last, predictors used in the statistical models may not be perfect to capture all attributions of REFB. For future work, bias estimation models will be constructed at higher resolutions with more RO profiles collected from the current FS7/C2 or other operational and commercial GNSS-RO satellites.

Author contribution: SY was in charge of the conceptualization of this study. SY and GP prepared the manuscript with contributions from all co-authors. GP constructed the packages of bias estimation. SY and GP analyzed the data. SY and GP wrote the manuscript draft; CC, SC, and CH reviewed and edited the manuscript. The authors greatly appreciate Dr. R. Anthes and the anonymous reviewer for insightful comments and suggestions for improving the manuscript.

Competing interests

The authors declare that they have no conflict of interest.

Acknowledgments

This work is supported by the Taiwan National Science and Technology Council grants NSTC-111-2121-M-008-001 and NSTC-111-2111-M-008-030 and Taiwan Space Agency grant TASA-S-110316.

Code and data availability

The codes of the bias estimators used in this study are available at Github (https://github.com/jiajia170801/bias_estimation_paper). The RO data is obtained from TDPC (TACC) by https://tacc.cwb.gov.tw/data-service/fs7rt_tdpc/. The ECMWF reanalysis v5 (ERA5) data is obtained from Copernicus server by https://cds.climate.copernicus.eu/cdsapp#!/dataset/reanalysis-era5-pressure-levels?tab=overview.

References

Anthes, R., Sjoberg, J., Feng, X., and Syndergaard, S.: Comparison of COSMIC and COSMIC-2 Radio Occultation Refractivity and Bending Angle Uncertainties in August 2006 and 2021, Atmosphere, 13, https://doi.org/10.3390/atmos13050790, 2022.

Ao, C., Chan, T., Iijima, B., Li, J., Mannucci, A., Teixeira, J., Tian, B., and Waliser, D.: Planetary boundary layer information from GPS radio occultation measurements, GRAS SAF Workshop on Applications of GPSRO Measurements, 123-131, 2008.

Bowler, N. E.: Revised GNSS-RO observation uncertainties in the Met Office NWP system, Q. J. R. Meteorol. Soc., 146, 2274-2296, https://doi.org/10.1002/qj.3791, 2020.

Bowler, N. E. : An assessment of GNSS radio occultation data produced by Spire, Q. J. R. Meteorol. Soc., 146, 3772-3788, https://doi.org/10.1002/qj.3872, 2020.

Chang, C.-C. and Yang, S.-C.: Impact of assimilating Formosat-7/COSMIC-II GNSS radio occultation data on heavy rainfall prediction in Taiwan, Terr. Atmos. Ocean. Sci., 33, https://doi.org/10.1007/s44195-022-00004-4, 2022.

Chen, S.-Y., Kuo, Y.-H., and Huang, C.-Y.: The Impact of GPS RO Data on the Prediction of Tropical Cyclogenesis Using a Nonlocal Observation Operator: An Initial Assessment, Mon. Weather Rev., 148, 2701-2717, 10.1175/mwr-d-19-0286.1, 2020.

Chen, S.-Y., Shih, C.-P., Huang, C.-Y., and Teng, W.-H.: An Impact Study of GNSS RO Data on the Prediction of Typhoon Nepartak (2016) Using a Multi-resolution Global Model with 3D-Hybrid Data Assimilation. Weather Forecast., 36, https://doi.org/10.1175/waf-d-20-0175.1, 2021a.

Chen, S.-Y., T.-C. Nguyen, and C.-Y. Huang: Impact of Radio Occultation Data on the Prediction of Typhoon Haishen (2020) with WRFDA Hybrid Assimilation. Atmosphere, 12, 1397. https://doi.org/10.3390/atmos12111397, 2021b.

Chen, S.-Y., Liu, C.-Y., Huang, C.-Y., Hsu, S.-C., Li, H.-W., Lin, P.-H., Cheng, J.-P., and Huang, C.-Y.: An Analysis Study of FORMOSAT-7/COSMIC-2 Radio Occultation Data in the Troposphere, Remote Sens., 13, https://doi.org/10.3390/rs13040717, 2021c.

Chen, Y.-J., Hong, J.-S., and Chen, W.-J.: Impact of Assimilating FORMOSAT-7/COSMIC-2 Radio Occultation Data on Typhoon Prediction Using a Regional Model, Atmosphere, 13, 10.3390/atmos13111879, 2022.

Chien, F. C., Hong, J. S., and Kuo, Y. H.: The Marine Boundary Layer Height over the Western North Pacific Based on GPS Radio Occultation, Island Soundings, and Numerical Models, Sensor-Basel, 19, https://doi.org/10.3390/s19010155, 2019.

Clarizia, M. P., Ruf, C. S., Jales, P., and Gommenginger, C.: Spaceborne GNSS-R Minimum Variance Wind Speed Estimator, IEEE. T. Geosci. Remote, 52, 6829-6843, https://doi.org/10.1109/tgrs.2014.2303831, 2014.

Cucurull, L.: Improvement in the Use of an Operational Constellation of GPS Radio Occultation Receivers in Weather Forecasting, Weather Forecast, 25, 749-767, https://doi.org/10.1175/2009waf2222302.1, 2010.

Cucurull, L. and Mueller, M. J.: An Analysis of Alternatives for the COSMIC-2 Constellation in the Context of Global Observing System Simulation Experiments, Weather Forecast, 35, 51-66, https://doi.org/10.1175/waf-d-19-0185.1, 2020.

Cucurull, L., Li, R., and Peevey, T. R.: Assessment of Radio Occultation Observations from the COSMIC-2 Mission with a Simplified Observing System Simulation Experiment Configuration, Mon. Weather Rev., 145, 3581-3597, https://doi.org/10.1175/mwr-d-16-0475.1, 2017.

Cucurull, L., Derber, J. C., Treadon, R., and Purser, R. J.: Assimilation of Global Positioning System Radio Occultation Observations into NCEP's Global Data Assimilation System, Mon. Weather Rev., 135, 3174-3193, https://doi.org/10.1175/mwr3461.1, 2007.

Eyre, J.: Assimilation of radio occultation measurements into a numerical weather prediction system, ECMWF Technical Memorandum, 34, https://doi.org/10.21957/r8zjif4it, 1994.

Feng, X., Xie, F., Ao, C. O., and Anthes, R. A.: Ducting and Biases of GPS Radio Occultation Bending Angle and Refractivity in the Moist Lower Troposphere, J. Atmos. Ocean. Tech., 37, 1013-1025, https://doi.org/10.1175/jtech-d-19-0206.1, 2020.

Fertig, E. J., Hunt, B. R., Ott, E., and Szunyogh, I.: Assimilating non-local observations with a local ensemble Kalman filter, Tellus A, 59, https://doi.org/10.1111/j.1600-0870.2007.00260.x, 2007.

Gorbunov, M. E.: Canonical transform method for processing radio occultation data in the lower troposphere, Radio Sci., 37, 9-1-9-10, https://doi.org/10.1029/2000rs002592, 2002.

Gorbunov, M. E. and Lauritsen, K. B.: Analysis of wave fields by Fourier integral operators and their application for radio occultations, Radio Sci., 39, https://doi.org/10.1029/2003rs002971, 2004.

Gorbunov, M. E., Vorob'ev, V. V., and Lauritsen, K. B.: Fluctuations of refractivity as a systematic error source in radio occultations, Radio Sci., 50, 656-669, https://doi.org/10.1002/2014rs005639, 2015.

Gorbunov, M. E., Lauritsen, K. B., Rhodin, A., Tomassini, M., and Kornblueh, L.: Radio holographic filtering, error estimation, and quality control of radio occultation data, J. Geophys. Res.-Atmos., 111, https://doi.org/10.1029/2005jd006427, 2006.

Healy, S. B.: Forecast impact experiment with a constellation of GPS radio occultation receivers, Atmos. Sci. Lett., 9, 111-118, https://doi.org/10.1002/asl.169, 2008.

Healy, S.: Assimilation in the upper-troposphere and lower-stratosphere: The role of GPS radio occultation, Seminar on Use of Satellite Observations in Numerical Weather Prediction, Shinfield Park, Reading, 2014.

Hsu, S. A.: Coastal Meteorology, Encyclopedia of Physical Science and Technology (Third Edition), 155-173, 2003.

Jensen, A. S., Lohmann, M. S., Benzon, H.-H., and Nielsen, A. S.: Full Spectrum Inversion of radio occultation signals, Radio Sci., 38, https://doi.org/10.1029/2002rs002763, 2003.

Jensen, A. S., Lohmann, M. S., Nielsen, A. S., and Benzon, H.-H.: Geometrical optics phase matching of radio occultation signals, Radio Sci., 39, https://doi.org/10.1029/2003rs002899, 2004.

Jensen, A. S., Benzon, H.-H., Nielsen, A. S., Marquardt, C., and Lohmann, M. S.: Evaluation of the Processing of Radio Occultation Signals by Reconstruction of the Real Signals, in: Atmosphere and Climate: Studies by Occultation Methods, edited by: Foelsche, U., Kirchengast, G., and Steiner, A., Springer Berlin Heidelberg, Berlin, Heidelberg, 113-125, https://doi.org/10.1007/3-540-34121-8_10, 2006.

Kuo, Y.-H., Wee, T.-K., Sokolovskiy, S., Rocken, C., Schreiner, W., Hunt, D., and Anthes, R. A.: J. Meteorol. Soc. Jpn., 82, 507–531, https://doi.org/10.2151/jmsj.2004.507, 2004.

Lien, G.-Y., Lin, C.-H., Huang, Z.-M., Teng, W.-H., Chen, J.-H., Lin, C.-C., Ho, H.-H., Huang, J.-Y., Hong, J.-S., Cheng, C.-P., and Huang, C.-Y.: Assimilation Impact of Early FORMOSAT-7/COSMIC-2 GNSS Radio Occultation Data with Taiwan's CWB Global Forecast System, Mon. Weather Rev., https://doi.org/10.1175/mwr-d-20-0267.1, 2021.

Liu, H., Kuo, Y. H., Sokolovskiy, S., Zou, X., and Zeng, Z.: Analysis bias induced in assimilation of the radio occultation bending angle with complex structures in the tropical troposphere, Q. J. R. Meteorol. Soc., 146, 4030-4037, https://doi.org/10.1002/qj.3887, 2020.

Liu, H., Kuo, Y.-H., Sokolovskiy, S., Zou, X., Zeng, Z., Hsiao, L.-F., and Ruston, B. C.: A Quality Control Procedure Based on Bending Angle Measurement Uncertainty for Radio Occultation Data Assimilation in the Tropical Lower Troposphere, J. Atmos. Ocean. Tech., 35, 2117-2131, https://doi.org/10.1175/jtech-d-17-0224.1, 2018.

Rennie, M. P.: The impact of GPS radio occultation assimilation at the Met Office, Q. J. R. Meteorol. Soc., 136, 116-131, https://doi.org/10.1002/qj.521, 2010.

Rocken, C., Anthes, R., Exner, M., Hunt, D., Sokolovskiy, S., Ware, R., Gorbunov, M., Schreiner, W., Feng, D., Herman, B., Kuo, Y. H., and Zou, X.: Analysis and validation of GPS/MET data in the neutral atmosphere, J. Geophys. Res.-Atmos., 102, 29849-29866, https://doi.org/10.1029/97jd02400, 1997.

Sjoberg, J., R.A. Anthes and H. Zhang, 2023: Estimating individual radio occultation uncertainties using the observations and environmental parameters. *J. Atmos. and Ocean Tech*., **40** (accepted for publication 8-28-23).

Schreiner, W., Sokolovskiy, S., Hunt, D., Rocken, C., and Kuo, Y. H.: Analysis of GPS radio occultation data from the FORMOSAT-3/COSMIC and Metop/GRAS missions at CDAAC, Atmos. Meas. Tech., 4, 2255-2272, https://doi.org/10.5194/amt-4-2255-2011, 2011.

Schreiner, W. S., Weiss, J. P., Anthes, R. A., Braun, J., Chu, V., Fong, J., Hunt, D., Kuo, Y. H., Meehan, T., Serafino, W., Sjoberg, J., Sokolovskiy, S., Talaat, E., Wee, T. K., and Zeng, Z.: COSMIC-2 Radio Occultation Constellation: First Results, Geophys. Res. Lett., 47, https://doi.org/10.1029/2019gl086841, 2020.

Sokolovskiy, S.: Effect of superrefraction on inversions of radio occultation signals in the lower troposphere, Radio Sci., 38, https://doi.org/10.1029/2002rs002728, 2003.

Sokolovskiy, S., Rocken, C., Schreiner, W., and Hunt, D.: On the uncertainty of radio occultation inversions in the lower troposphere, J. Geophys. Res., 115, https://doi.org/10.1029/2010jd014058, 2010.

Sokolovskiy, S., W. Schreiner, Z. Zeng, D. Hunt, Y.-C. Lin, and Y.-H. Kuo: Observation, analysis, and modeling of deep radio occultation signals: Effects of tropospheric ducts and interfering signals, Radio Sci., 49, 954–970, doi:10.1002/ 2014RS005436, 2014.

Sokolovskiy, S., Zeng, Z., Hunt, D., Weiss, J.-P., Braun, J., Schreiner, W., Anthes, R., Kuo, Y.-H., Zhang, H., Lenschow, D., and VanHove, T.: Detection of super-refraction at the top of the atmospheric boundary layer from COSMIC-2 radio occultations. J. Atmos. and Ocean Tech., 40, 65-78. https://doi.org/10.1175/JTECH-D-22-0100.1, 2024.

Tatarskiy, V. I.: Determining atmospheric density from satellite phase and refraction-angle measurements, Izv. Atmos. Oceanic Phys., 4, 401-406, 1968.

Wang, K.-N., Ao, C., and de la Torre Juárez, M.: GNSS-RO Refractivity Bias Correction Under Ducting Layer Using Surface-Reflection Signal, Remote Sens., 12, https://doi.org/10.3390/rs12030359, 2020.

Wang, K.-N., de la Torre Juárez, M., Ao, C. O., and Xie, F.: Correcting negatively biased refractivity below ducts in GNSS radio occultation: an optimal estimation approach towards improving planetary boundary layer (PBL) characterization, Atmos. Meas. Tech., https://doi.org/10, 4761-4776, 10.5194/amt-10-4761-2017, 2017.

Wee, T.-K., Anthes, R.A., Hunt, D.C., Schreiner, W.S., Kuo, Y.-H.: Atmospheric GNSS RO 1D-Var in Use at UCAR: Description and Validation, *Remote Sens*., **14**, 5614. https://doi.org/10.3390/rs14215614, 2022.

Xie, F., Syndergaard, S., Kursinski, E. R., and Herman, B. M.: An Approach for Retrieving Marine Boundary Layer Refractivity from GPS Occultation Data in the Presence of Superrefraction, J. Atmos. Ocean. Tech., 23, 1629-1644, https://doi.org/10.1175/JTECH1996.1, 2006.

Xie, F., Wu, D. L., Ao, C. O., Kursinski, E. R., Mannucci, A. J., and Syndergaard, S.: Super-refraction effects on GPS radio occultation refractivity in marine boundary layers, Geophys. Res. Lett., 37, https://doi.org/10.1029/2010gl043299, 2010.

Xie, F, Visiting Scientist Report 21: Investigation of methods for the determination of the PBL height from RO observations using ECMWF reanalysis data, SAF/ROM/DMI/REP/VS21/001, 2014.

Yang, J., Wang, Z., Heymsfield, A. J., and French, J. R.: Characteristics of vertical air motion in isolated convective clouds, Atmos. Chem. Phys., 16, 10159-10173, https://doi.org/10.5194/acp-16-10159-2016, 2016.

Yang, S.-C., Chen, S.-H., Chen, S.-Y., Huang, C.-Y., and Chen, C.-S.: Evaluating the Impact of the COSMIC RO Bending Angle Data on Predicting the Heavy Precipitation Episode on 16 June 2008 during SoWMEX-IOP8, Mon. Weather Rev., 142, 4139-4163, https://doi.org/10.1175/mwr-d-13-00275.1, 2014.

Zhang, H., Kuo, Y.-H., and Sokolovskiy, S.: Assimilation of Radio Occultation Data Using Measurement-Based Observation Error Specification: Preliminary Results, Mon. Weather Rev., 151, 589-601, https://doi.org/10.1175/mwr-d-22-0122.1, 2023.

Table 1: Correlation coefficients between the mean real and estimated REFBs below 1.5 km over ocean and land in Southern Hemisphere (SH) and Northern Hemisphere

Correlation coefficients	**LSW based**		***TQ* based**	
	Ocean (SH/NH)	Land (SH/NH)	Ocean (SH/NH)	Land (SH/NH)
Training data set	0.94/0.96	0.9/0.92	0.79/0.75	0.72/0.69
Testing data set	0.93/0.96	0.89/0.87	0.71/0.68	0.70/0.63

Table 2: Global mean RMSE of each REFB estimation in comparison to the real REFB below 1.5 km

Global mean RMSE	**LSW-based**	***T*Q-based**	**MVE**
Training data set	2.033	1.614	1.088
Testing data set	2.815	2.266	1.731

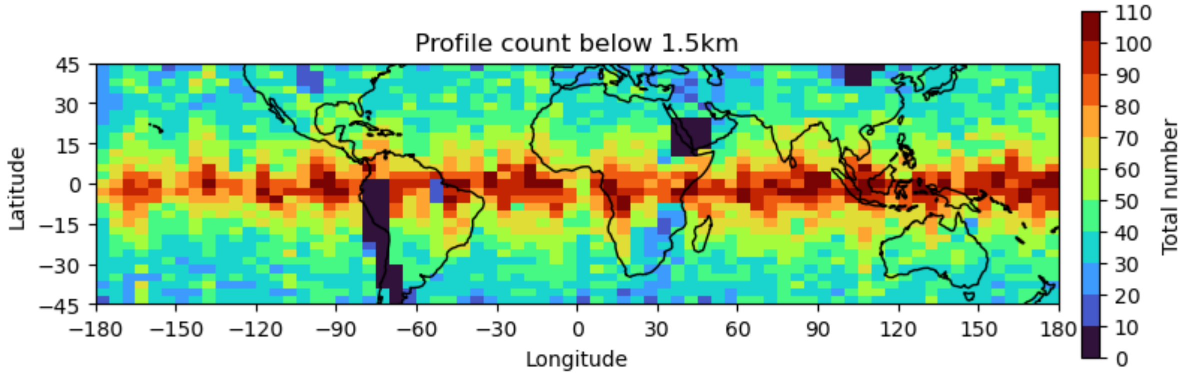

Figure 1: Number of FS7/C2 RO profiles below the 1.5 km height during the study period (unit: number of profiles).

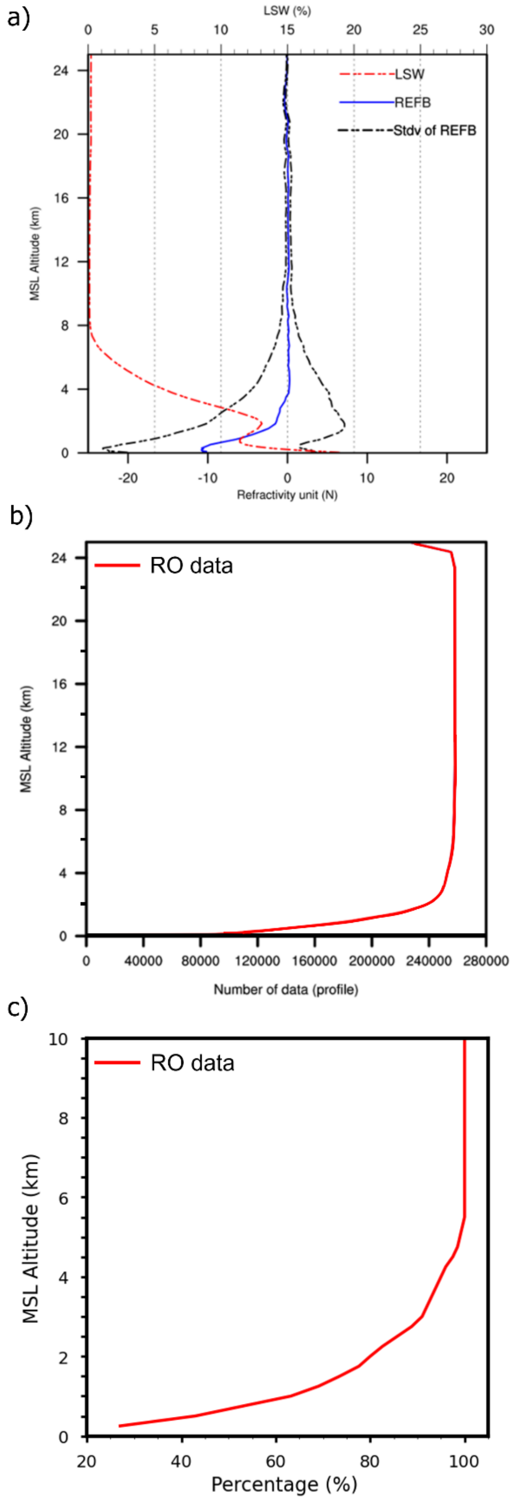

Figure 2: (a) Mean and standard deviation of REFB and mean LSW as a function of height. (b) The amount of available RO data, and (c) the percentage of profiles as a function of height in reference to the total number at 10 km. The RO data are from 1st December 2019 to 29th February 2020.

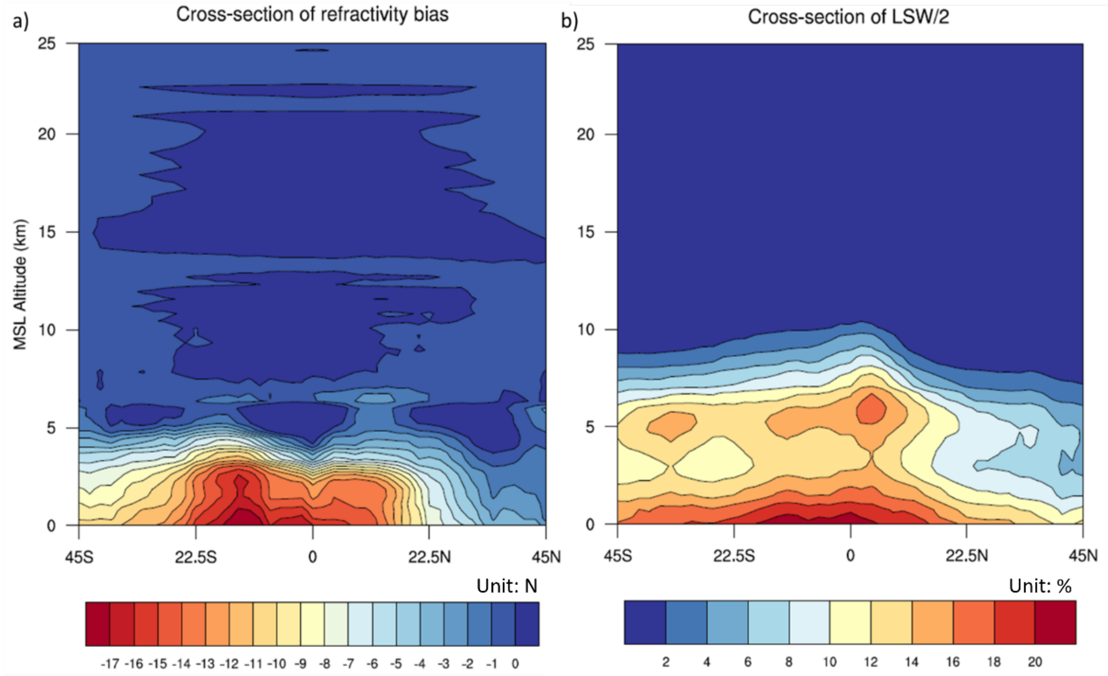

Figure 3: The cross-sections of (a) zonal mean REFB and (b) mean LSW/2 from 1st December 2019 to 29th February 2020.

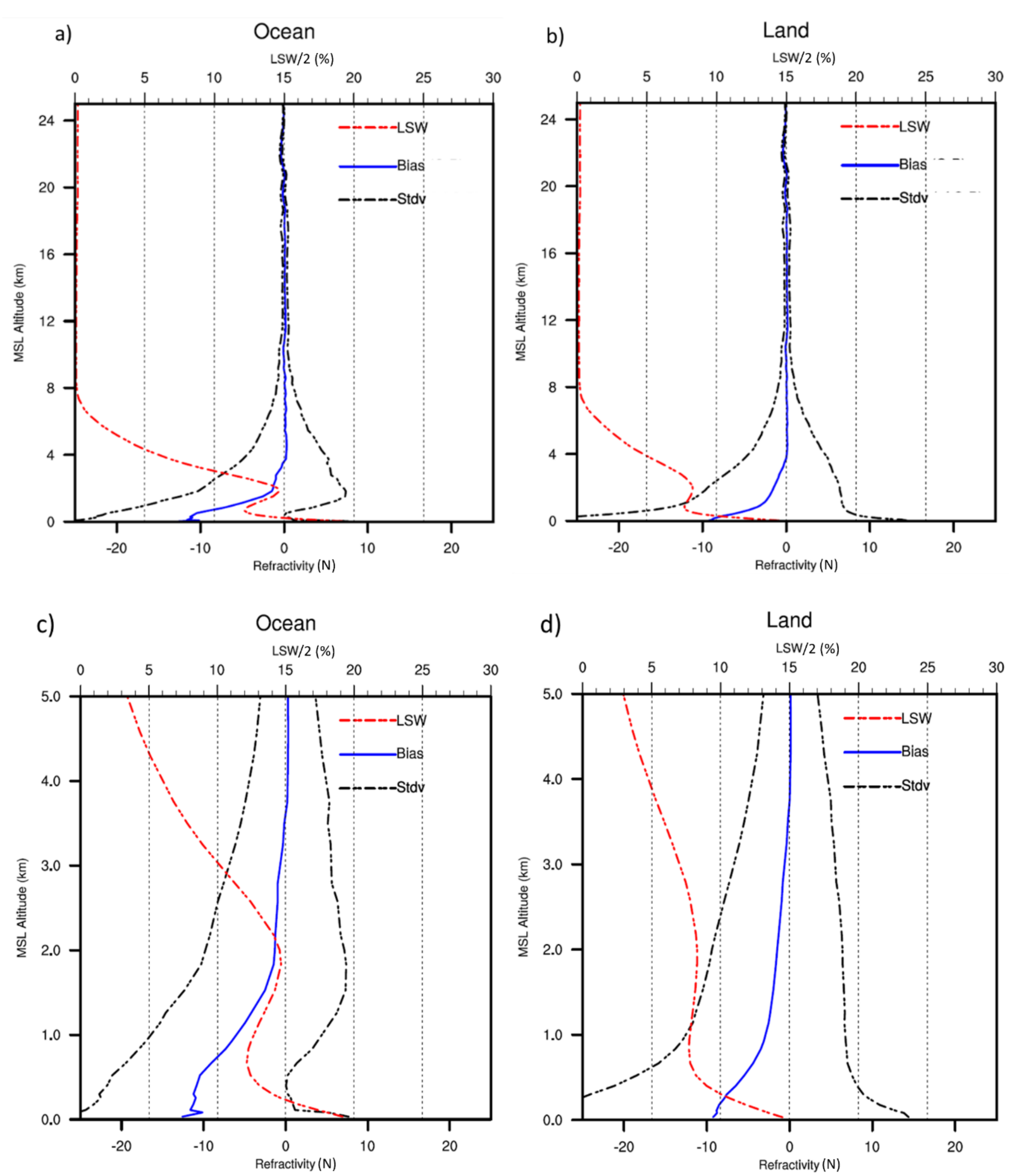

Figure 4: (a) and (b) are vertical profiles of the mean and standard deviation of REFB, and mean LSW with altitudes up to 25 km over ocean and land, respectively. (c) and (d) are the same as (a) and (b) except zoomed versions below 5 km.

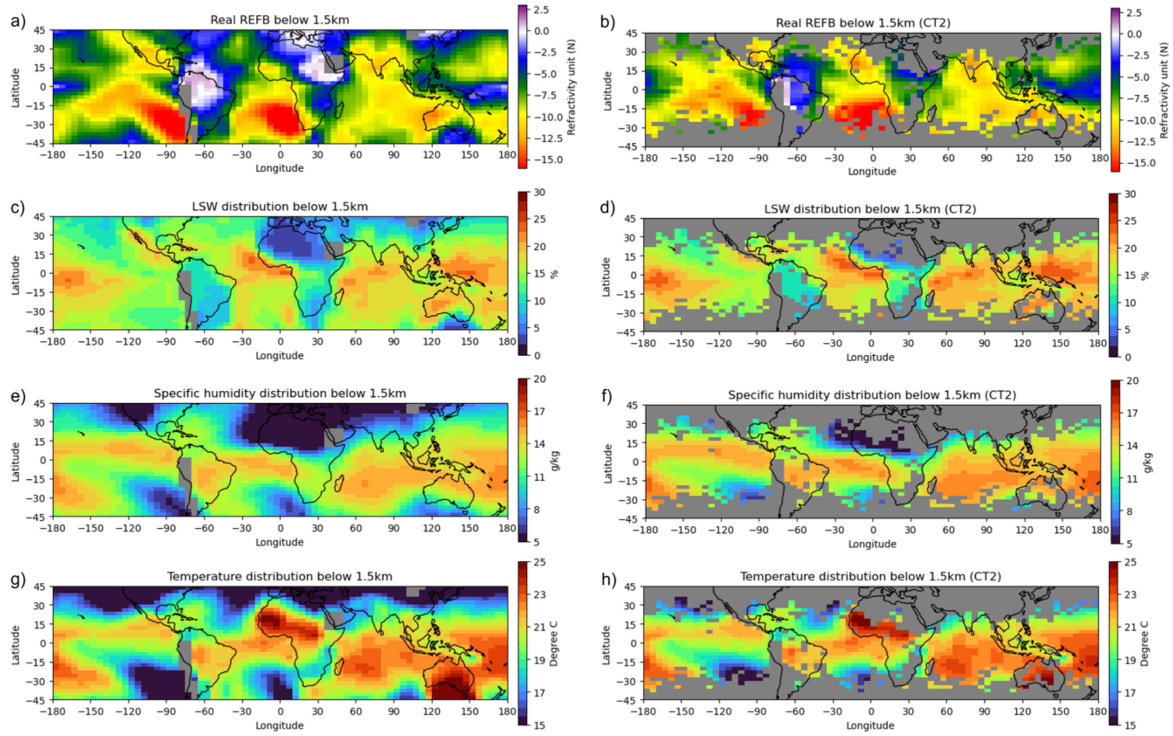

Figure 5: Horizontal distribution of (a) REFB (*N units*), (c) LSW (%), (e) specific humidity (g kg^{-1}), and (g) temperature (°C) during the study period. The values of REFB, LSW, specific humidity and temperature are averages over the lowest 1.5 km MSL of the atmosphere. (b), (d), (f) and (h) are the same as (c), (c), (e) and (g), but they are calculated with the criterion that at least 30 profiles penetrate below 0.5 km in each box.

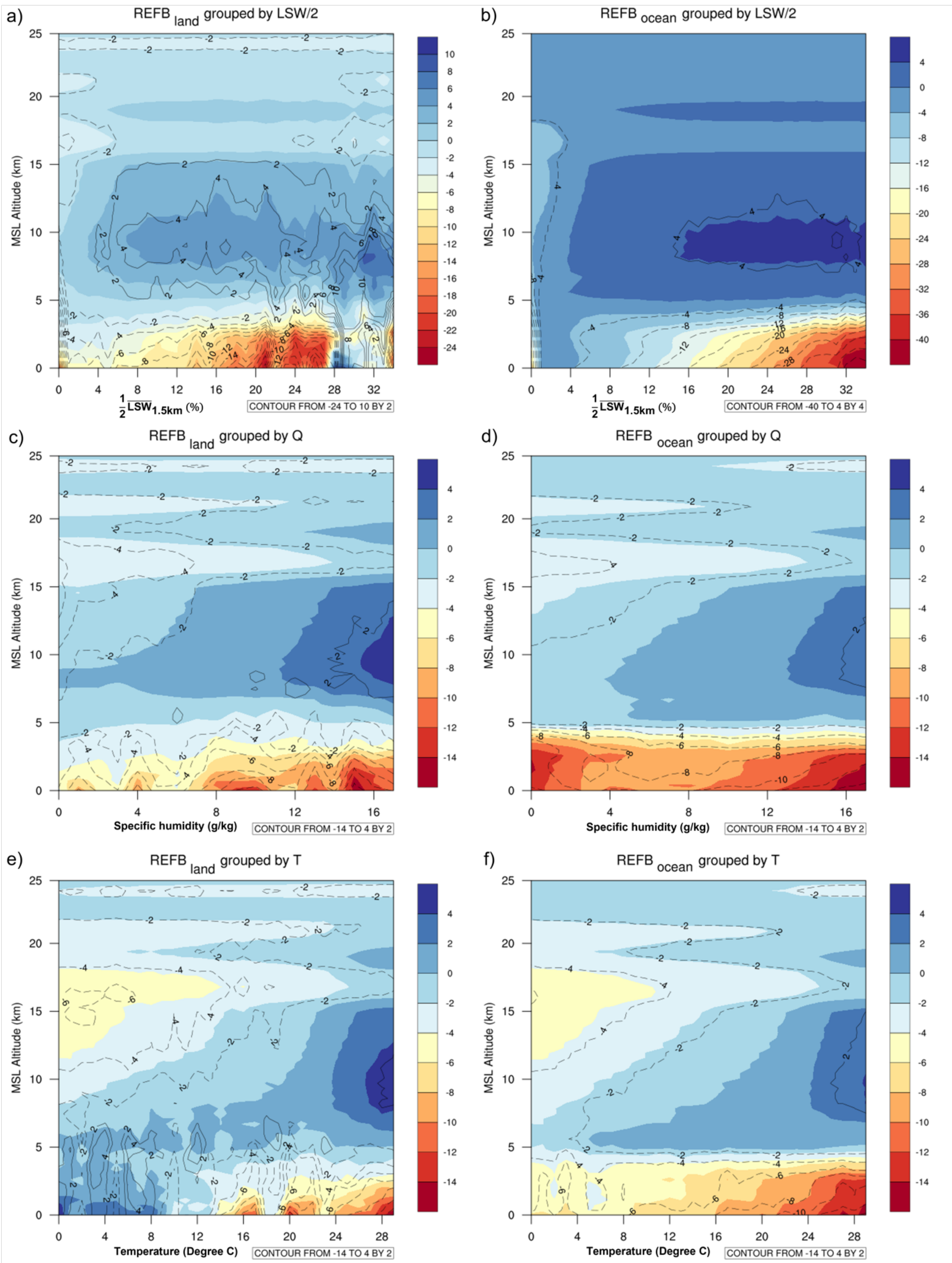

Figure 6: Refractivity bias as a function of height and average values over the lowest 1.5 km above MSL of (a) LSW/2, (c) specific humidity and (e) temperature over land. (b), (d) and (f) are the same as (a), (c) and (e), except over the ocean. The color shading shows the result using the RO profiles penetrating below 1.5 km while the contour uses the RO profiles penetrating below 0.5 km.

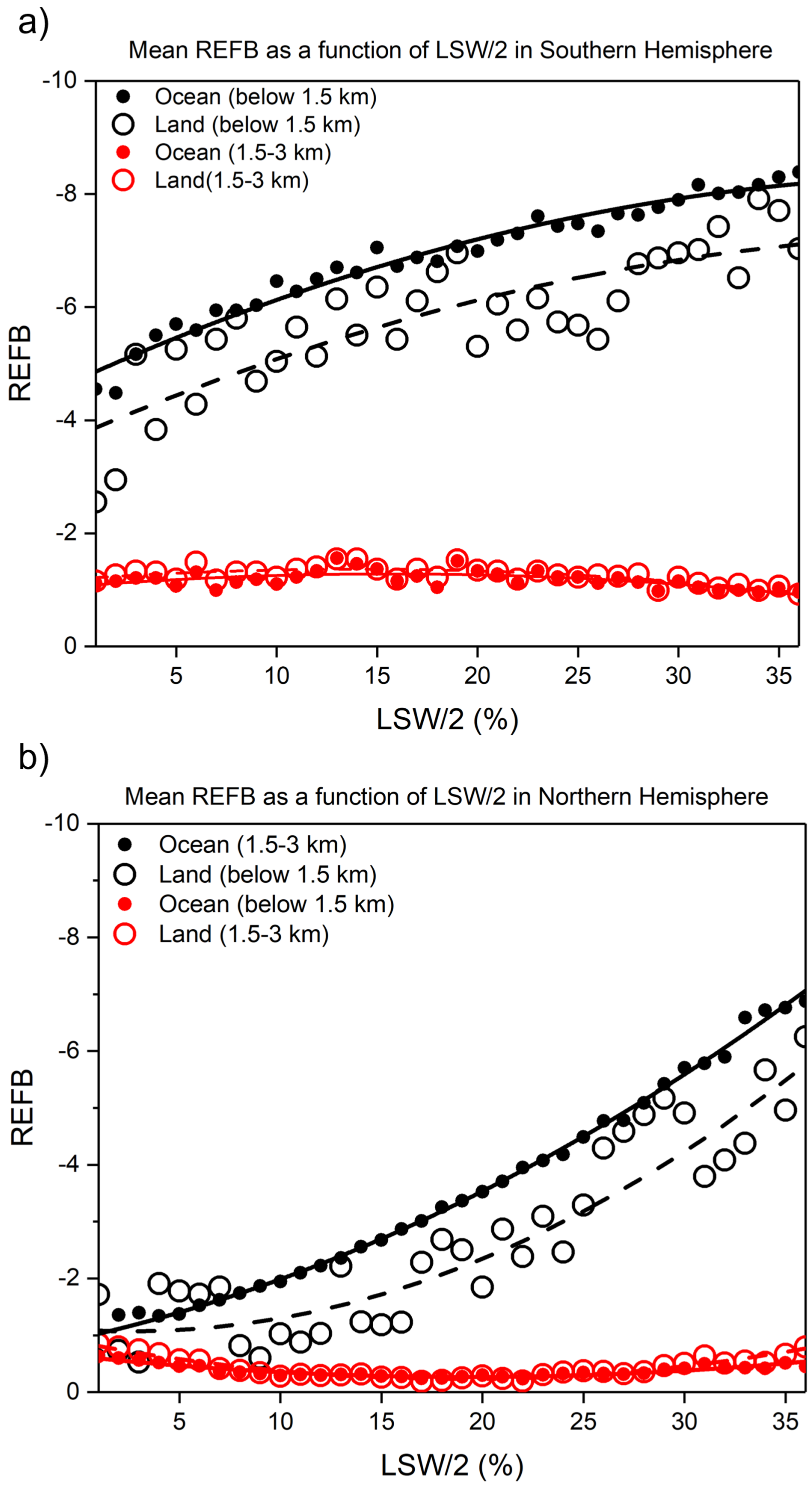

Figure 7: Relationship between LSW/2 and REFB. The solid and dashed lines represent the REFB computed from the statistical model for the ocean and land, respectively, as a function of LSW/2 (Southern Hemisphere only). LSW/2 and REFB are averaged below 1.5 km.

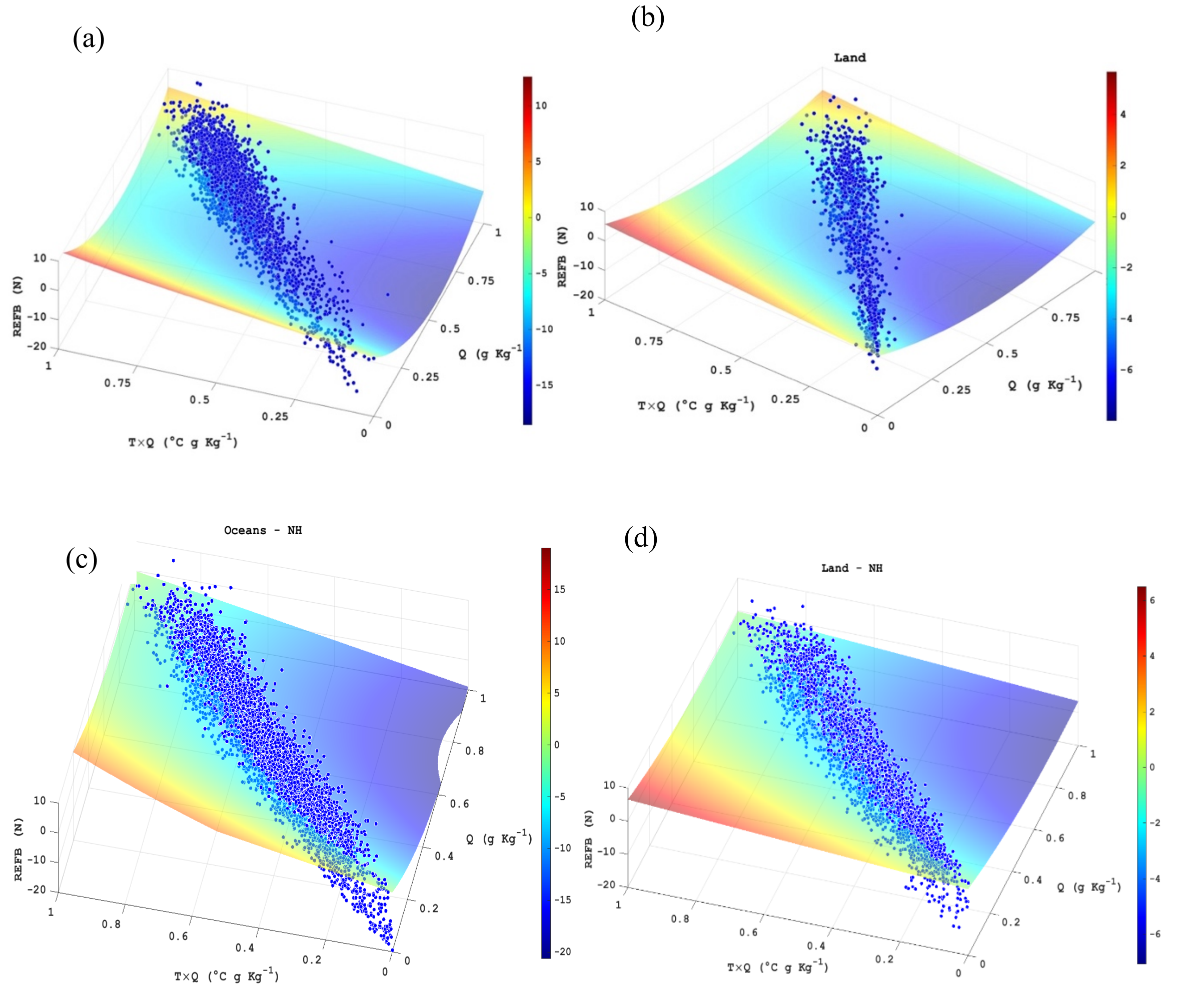

Figure 8: The relationship among REFB, normalized specific humidity, product of normalized temperature and normalized specific humidity of a) oceans and b) land in the Southern Hemisphere. The scatters are the averaged values of each profile below the lowest 1.5 km MSL. The surfaces show the model computed from statistical model (Eq. 3) as the function of normalized specific humidity and product of normalized temperature and humidity. (c) and (d) are the same as (a) and (b), but for the Northern Hemisphere.

676 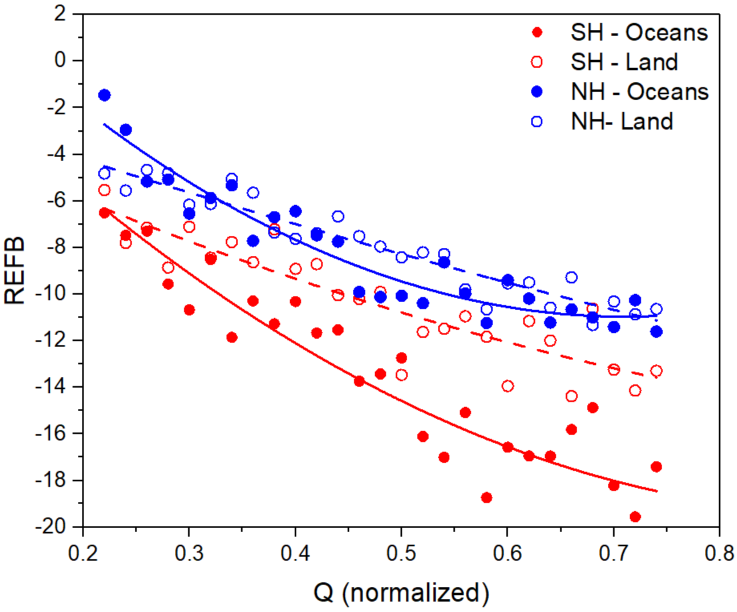

677 **Figure 9: The relationship between REFB and normalized Q given a condition of normalized *TQ*=0.5.**

678

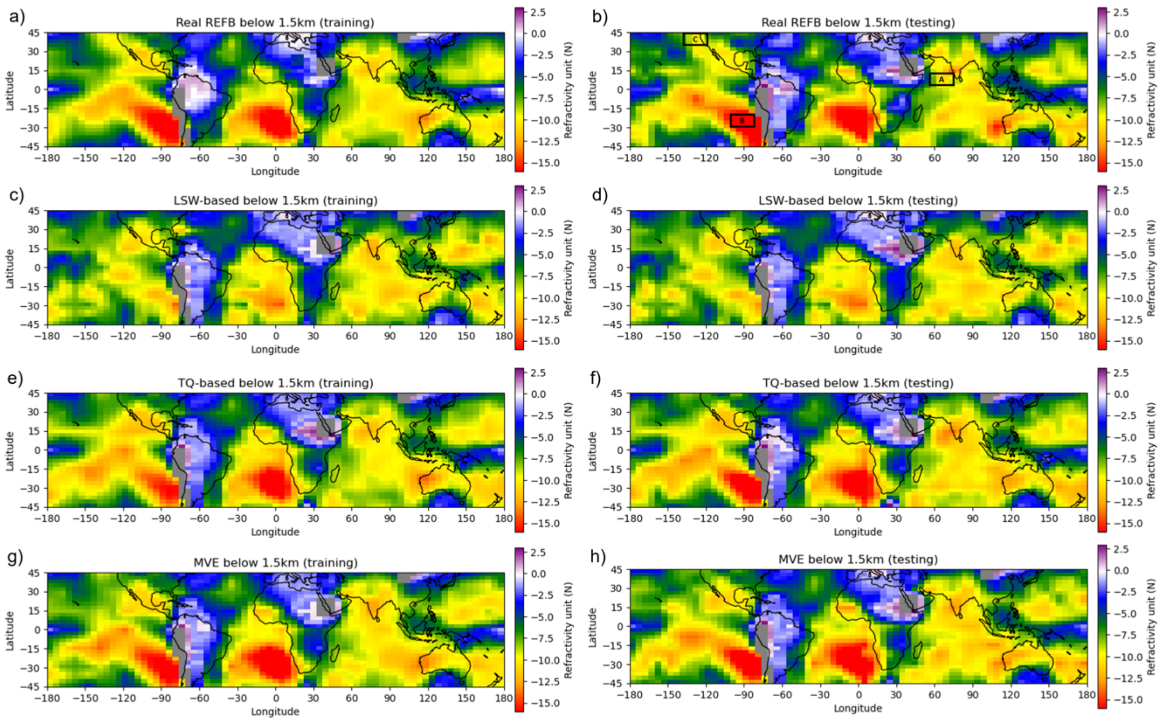

Figure 10: Horizontal distribution of refractivity bias and different estimated refractivity biases. The boxes denoted A and B are the example boxes used in Figures 12 and 13, respectively. All variables used to construct this figure are averaged below 1.5km. Area A is in the region of 0° < Lat < 10°N and 55°E < Lon <75°E, Area B is in the region of 20°S < Lat < 30°S and 105°W < Lon < 85°W, and Area C is in the region of 35°S < Lat < 45°S and 120°W < Lon < 135°W.

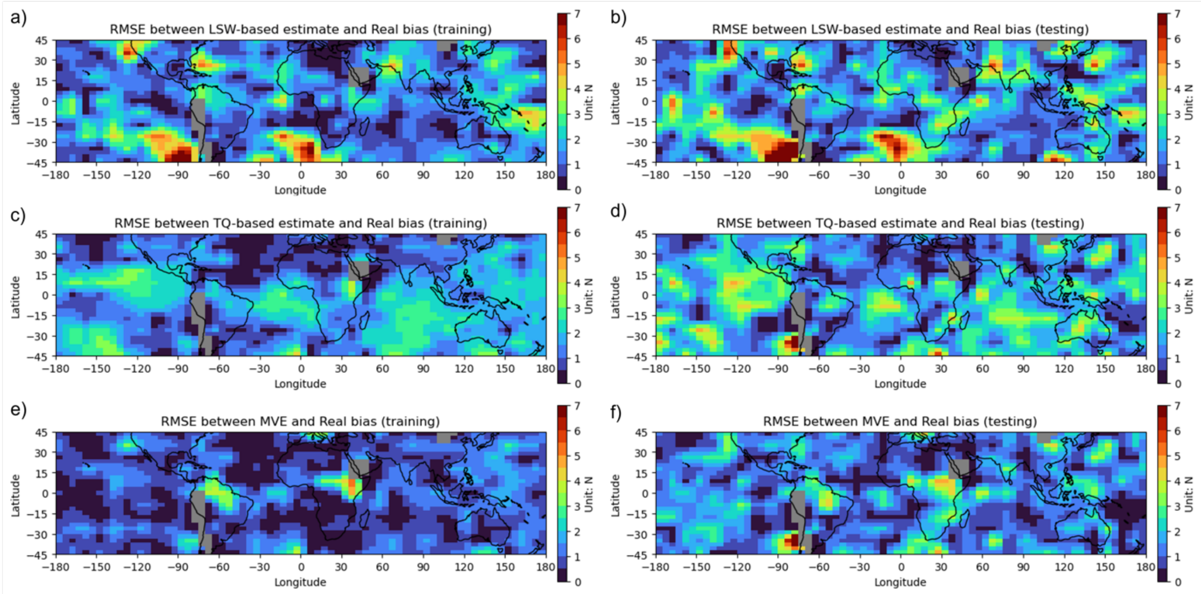

Figure 11: Horizontal distribution of RMSE between the real REFB and estimated REFB by different methods with training (left column) and testing (right column) data.

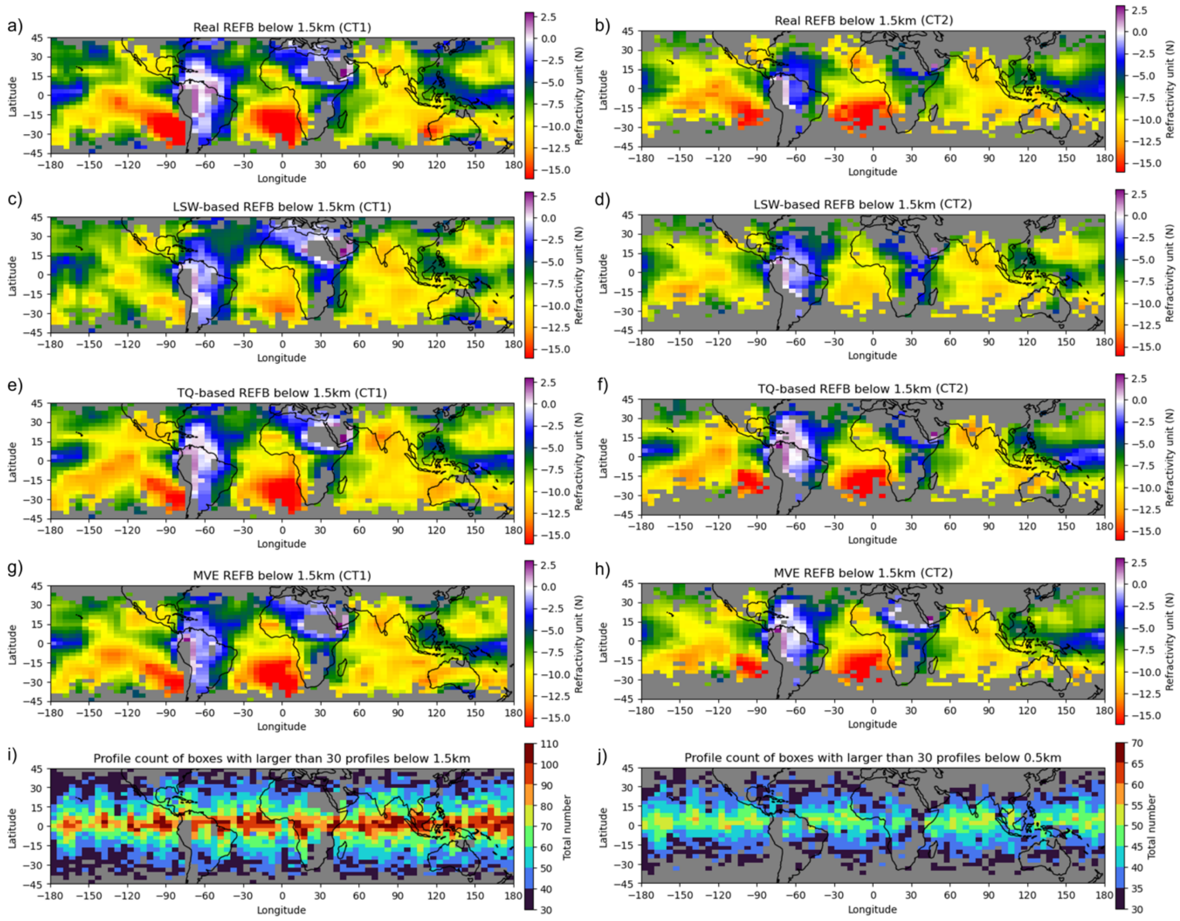

Figure 12: The same as Fig. 10, but the calculation is done for RO data with different criteria (CT1 and CT2) of sample selection. CT1 requires at least 30 RO profiles penetrate below 1.5 km in each box, and CT2 is the same as CT2 except that the profiles penetrate 0.5 km. (i) and (j) are the horizontal distribution of the profile count with criterion CT1 and CT2, respectively.

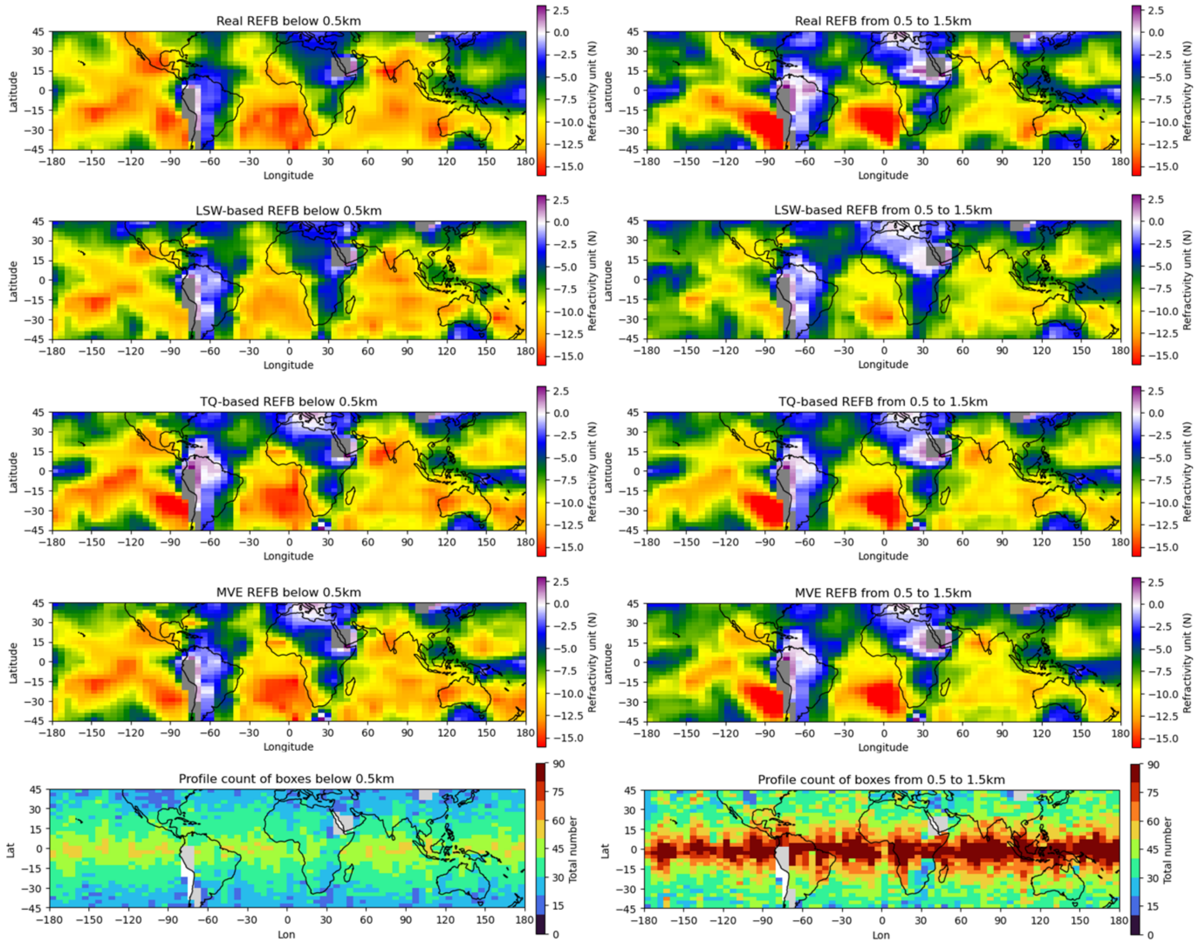

Figure 13: The same as Fig. 10, but the calculation is done for RO data from different levels. The left column uses the data below 0.5 km and the right column use the data between 0.5 and 1.5 km. (i) and (j) are the horizontal distribution of the profile count below 0.5km and between 0.5 and 1.5 km, respectively.

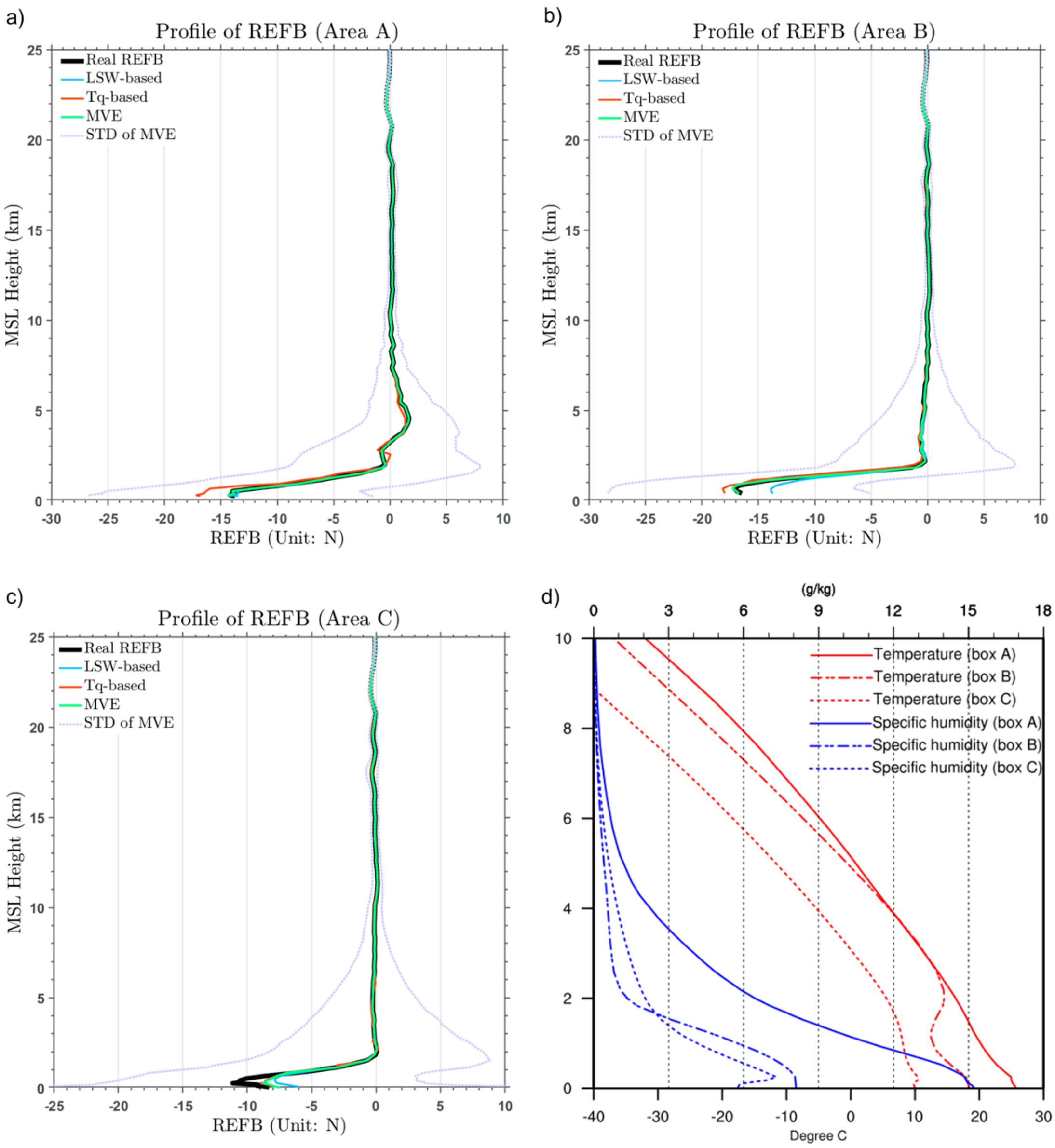

Figure 14: Profiles of refractivity bias (real and estimates) for two different areas selected in Fig. 10a. Boxes A, B and C are in (0° < Lat < 10°N, 55°E < Lon <75°E) and (20°S < Lat < 30°S, 105°W < Lon < 85°W) and (35°S < Lat < 45°S and 120°W < Lon < 135°W). (d) Profiles of temperature (red lines) and specific humidity (blue lines) averaged for Areas A (solid lines), B (long-dashed lines) and C (short-dashed line) shown in Fig. 10b.